Green Chemical Technology

SCIEPublish

Article

Synthesis of Hydroxyapatite Porous Microspheres for Efficient Adsorption of Copper Ion from Water

Tengfei Ding [1], Ruan Chi [2], Junxia Yu [1,3], Weiyan Yin [4], Zhongzheng Hu [1,*] and Qingbiao Zhao [1,2,3,*]

[1] School of Chemistry and Environmental Engineering, Wuhan Institute of Technology, Wuhan 430205, China; 22309010086@stu.wit.edu.cn (T.D.); 08090201@wit.edu.cn (J.Y.)
[2] Hubei Three Gorges Laboratory, No. 1 Mazongling Rd, Xiaoting District, Yichang 443007, China; rac@wit.edu.cn (R.C.)
[3] State Key Laboratory of Green and Efficient Development of Phosphorous Resources, Wuhan 430205, China
[4] Key Laboratory of Textile Fiber and Products (Ministry of Education), School of Chemistry and Chemical Engineering, Wuhan Textile University, Wuhan 430020, China; 2016046@wtu.edu.cn (W.Y.)

* Corresponding author. E-mail: 25071116@wit.edu.cn (Z.H.); 23031701@wit.edu.cn (Q.Z.)

Received: 30 December 2025; Revised: 28 January 2026; Accepted: 1 April 2026; Available online: 13 April 2026

ABSTRACT: Copper is a common heavy metal contamination source for water bodies, and achieving sustainable and cost-effective removal of Cu^{2+} from Cu-containing wastewater remains a challenge. In this study, an economical and eco-friendly adsorbent—hydroxyapatite (HA) porous microspheres—was synthesized via a simple one-step hydrothermal method. Adsorption experiments demonstrated that the maximum adsorption capacity of HA porous microspheres for Cu^{2+} is 116 mg/g, approximately 3.74 times that of reported HA nanosheet adsorbents. The adsorption process follows the pseudo-second-order kinetic model and the Sips isotherm model. The correlation coefficient $R^2 = 0.9997$. Linear fitting of the amounts of Cu^{2+} removed and Ca^{2+} leached at the same time revealed an R^2 value as high as 0.997, indicating that ion exchange is the dominant adsorption mechanism. Therefore, the excellent adsorption performance is attributed to the high specific surface area (207 m^2/g) and mesoporous structure of the spherical HA adsorbent, which provides abundant active sites and promotes efficient ion diffusion. These structural advantages significantly enhanced the two primary adsorption mechanisms: ion exchange and surface complexation. Furthermore, the effects of adsorbent dosage, solution pH, reaction time, initial Cu^{2+} concentration, and temperature on adsorption performance were systematically investigated. Finally, the adsorption mechanism was investigated by characterizing the adsorbed material using XRD, FTIR, and XPS. It was determined that ion exchange, complexation, and electrostatic attraction are the main adsorption mechanisms. This study enhances the adsorption capacity of HA materials for Cu^{2+} by controlling morphology, offering new perspectives for developing high-performance, economical, eco-friendly, and sustainable adsorbents.

Keywords: Adsorption; Hydroxyapatite; Heavy metal; Ion exchange; Microsphere

1. Introduction

Copper (Cu) is extensively utilized in industrial production, including mining, smelting, electroplating, and circuit board printing [1–4]. With the acceleration of industrialization, the discharge of wastewater

containing Cu^{2+} ions has increased significantly [5]. Such industrial wastewater is highly toxic, non-degradable, and subject to bioaccumulation [6–9]. The direct release of Cu-containing wastewater not only seriously threatens ecological security and human health, but also causes huge resource loss [10]. Correspondingly, researchers have developed adsorption, precipitation, reverse osmosis, and membrane filtration methods to remove Cu^{2+} ions from wastewater [11].

Among them, adsorption is a predominant technique due to its high efficiency, low cost, and operational simplicity. So far, various adsorbents, such as metal-organic frameworks (MOFs) [12], activated carbon [13], and graphene [14], have been extensively investigated and applied. Rodríguez et al. [15] investigated the adsorption effect of Co-derived metal-organic framework (Co-MOF) on different heavy metals. The results showed that Co-MOF had an adsorption capacity of 75.47 mg/g for copper. Amara et al. [16] prepared composite beads of chitosan and amidoxime grafted graphene oxide, achieving an adsorption efficiency of 12.96 mg/g within a 160 min adsorption time. However, their biosafety risks and high cost have hindered practical applications. Therefore, it is urgent to develop an economical, resource-saving, and eco-friendly adsorbent to treat Cu-contaminant wastewater efficiently.

Hydroxyapatite (HA, $Ca_{10}(PO_4)_6(OH)_2$) is a naturally occurring calcium phosphate mineral. Owing to its high surface reactivity, substantial ion-exchange capacity, and biocompatibility, HA has been regarded as an attractive candidate for the adsorption of Cu^{2+} ions [17–19]. However, HA materials prepared by traditional methods typically exhibit bulk or powder morphology, and insufficient active sites and particle agglomeration limit their adsorption capacity [20]. In recent years, rod-shaped, nanosheet-like, and tubelike structures of HA have been developed to enhance its adsorption performance by increasing surface functional groups (such as Ca^{2+}, PO_4^{3-}, OH^-) for ion exchange, surface complexation, and dissolution-precipitation reactions with heavy metal ions [19,21]. Despite numerous efforts, the adsorption performance is limited. For example, the adsorption capacity of HA nanosheets prepared by microwave-assisted hydrothermal method for Cu^{2+} was only 31.6 mg/g [22]. The effect was far less than that observed in the study by Rodríguez et al. [15]. Consequently, developing porous HA materials with higher specific surface areas, denser adsorption sites, and superior adsorption properties has become a key focus of current research.

In this study, HA porous microspheres with a high specific surface area were prepared using a simple one-step hydrothermal method to explore its adsorption capacity for Cu^{2+} ions. The factors, including adsorbent dosage, solution pH, reaction time, Cu^{2+} concentration, and temperature, were investigated to evaluate the practical application feasibility of the HA porous microspheres. Moreover, the adsorption mechanisms of Cu^{2+} onto the HA porous microspheres were thoroughly studied. This study provides a method for preparing pure spherical hydroxyapatite, which is expected to reduce medical side effects [23]. The excellent adsorption effect of this spherical hydroxyapatite on copper was then evaluated in depth, and its mechanism was elucidated through characterization, providing a theoretical basis for copper-loaded hydroxyapatite.

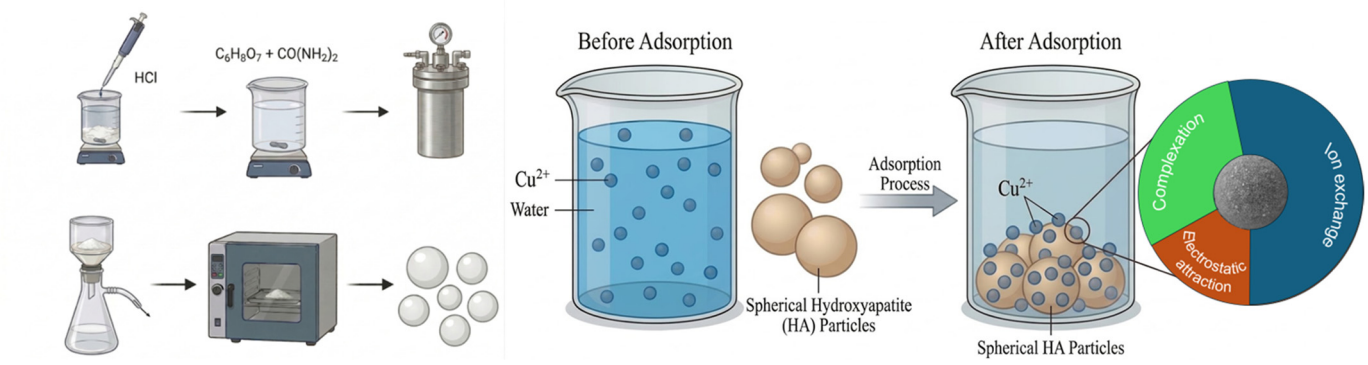

Schematic Diagram.

2. Materials and Methods

2.1. Chemicals and Materials

All the chemical reagents used in the experiment were analytical grade and were used without further purification. Calcium chloride dihydrate ($CaCl_2·2H_2O$, ≥99.0%), Sodium hydroxide (NaOH, ≥96.0%), Nitric acid (HNO_3), Magnesium Chloride Hexahydrate ($MgCl_2·6H_2O$, ≥98.0%), hydrochloric acid (HCl), and ethanol (C_2H_5OH) were provided by Sinopharm Chemical Reagent Co., Ltd. (Shanghai, China). Diammonium hydrogen phosphate ($(NH_4)_2HPO_4$, ≥99.0%), Sodium Chloride (NaCl, ≥99.9%) and Potassium Chloride (KCl, ≥99.9%) was purchased from GENERAL-REAGENT (Ringoes, NJ, USA). Citric acid monohydrate ($C_6H_8O_7·H_2O$, ≥99.5%), copper nitrate trihydrate ($Cu(NO_3)_2·3H_2O$, ≥99.0%), and urea (H_2NCONH_2, ≥99.0%) were purchased from ChengDu Chron Chemicals Co., Ltd. (Chengdu, China) Deionized water was obtained using an ultrapure water system (Ulupure).

2.2. Synthesis of Hydroxyapatite Porous Microspheres

Hydroxyapatite porous microspheres with a large specific surface area were prepared by a simple hydrothermal method. First, 1.176 g $CaCl_2·2H_2O$ was dissolved in 160 mL of deionized water, and 0.634 g $(NH_4)_2HPO_4$ was added to the solution, resulting in the formation of a white precipitate. The pH of the mixture was adjusted to 2.5 using 1 M HCl. Subsequently, 0.004 mol of $C_6H_8O_7·H_2O$ and 2.4 g of H_2NCONH_2 were successively added to the suspension. After stirring for 30 min, the suspension was transferred into a 100 mL Teflon-lined stainless-steel autoclave. The hydrothermal reaction was performed at 120 °C for 3 h. Finally, the resulting precipitate was collected, washed, and dried overnight to obtain the HA porous microspheres.

2.3. Characterizations

The morphology and elemental composition of the prepared samples were investigated and analyzed by a scanning electron microscope (SEM) (TESCAN MIRA LMS, Brno, Czech Republic) equipped with energy-dispersive X-ray spectroscopy (EDS). The phase identification and crystal structure were determined using X-ray diffraction (XRD) on a Rigaku-2038 diffractometer (Rigaku, Tokyo, Japan) at 25 °C with Cu-Kα radiation from 10 to 80 degrees at a scan rate of 5 degrees/min. FTIR spectra were collected on a Thermo Scientific Nicolet iS20 FTIR spectrometer (Thermo Fisher Scientific, Waltham, MA, USA). X-ray photoelectron spectroscopy (XPS) was performed on a Thermo Scientific ESCALAB 250 Xi instrument (Thermo Fisher Scientific, Waltham, MA, USA) to analyze the chemical states of the elements. The surface charge of the sample was measured with a zeta potential analyzer (Malvern Zetasizer Nano ZS90, Worcestershire, UK). The specific surface area was determined using the Brunauer-Emmett-Teller (BET) method on an ASAP 2460 instrument (Micromeritics, Norcross, GA, USA). The concentration of Cu^{2+} ions in the solution was quantified by atomic absorption spectrometry (Thermo ICE3300 FL AAS, Thermo Fisher Scientific, Waltham, MA, USA).

2.4. Adsorption Experiments

Typically, 0.04 g of HA was added to 50 mL of a Cu^{2+} ions solution (100 mg/L). The mixture was then shaken in a shaker at 25 °C and 180 rpm for 300 min. The effects of dosage (0.2–1.2 g/L) and solution pH (3–5) on adsorption performance were investigated to establish optimal adsorption conditions. For the kinetic studies, the initial Cu^{2+} concentration was set at 100 mg/L. Solution samples were withdrawn at predetermined time intervals, filtered through a 0.45 μm membrane filter, and then analyzed for the concentrations of Cu^{2+} and Ca^{2+}. The adsorption isotherms were obtained by conducting experiments with

different initial Cu^{2+} concentrations at an adsorption time of 300 min. Furthermore, thermodynamic parameters were studied at 308 K, 318 K, and 328 K, respectively.

2.5. Analysis Methods

The adsorption capacity (q_e) and removal (R, %) were calculated using the following equations (Equations (1) and (2)):

$$q_e = \frac{(C_0 - C_e) \times \mathrm{V}}{m} \tag{1}$$

$$\text{Remove (\%)} = \frac{C_0 - C_e}{C_0} \times 100\% \tag{2}$$

where C_0 and C_e (mg/L) represent the initial and equilibrium ion concentrations, respectively. V (L) is the volume of the solution, and m (g) is the mass of the adsorbent. The kinetic data were fitted using pseudo-first-order and pseudo-second-order models (Equations (3) and (4)).

$$\ln(q_e - q_t) = \ln q_e - k_1 t \tag{3}$$

$$\frac{t}{q_t} = \frac{1}{k_2 q_e^2} + \frac{t}{q_e} \tag{4}$$

where q_e and q_t are the adsorption capacity (mg/g) at equilibrium and time t, respectively. k_1 (1/min) and k_2 (g/(mg·min)) are the rate constants of the pseudo-first-order and pseudo-second-order models, respectively. The adsorption data were fitted to the Langmuir, Freundlich, and Sips isotherm models (Equations (5)–(7)) [24].

$$q_e = \frac{q_{max} K_L C_e}{1 + K_L C_e} \tag{5}$$

$$q_e = K_F C_e^{\frac{1}{n}} \tag{6}$$

$$q_e = \frac{q_{max} (K_s C_e)^{\frac{1}{m}}}{1 + (K_s C_e)^{\frac{1}{m}}} \tag{7}$$

where q_{max} represents the theoretical maximum adsorption capacity, K_L, K_F, and K_S denote the equilibrium constants for the Langmuir, Freundlich, and Sips models, respectively. n and m are the exponents in the Freundlich and Sips models, respectively. The spontaneity and thermodynamic behavior of Cu^{2+} adsorption on HA were evaluated by calculating Gibbs free energy change (ΔG°, kJ/mol), entropy change (ΔS°, J/(mol·K)), and enthalpy change (ΔH°, kJ/mol). The calculation equations were as follows (Equations (8)–(10)):

$$lnK_c = \frac{-\Delta \mathrm{H}^\circ}{RT} + \frac{\Delta \mathrm{S}^\circ}{R} \tag{8}$$

$$\Delta \mathrm{G}^\circ = -RTlnK_c \tag{9}$$

$$K_c = \frac{q_e}{C_e} \tag{10}$$

where R (8.314 J/(K·mol)) is the gas constant, K_c is the thermodynamic equilibrium constant, and T (K) is the absolute temperature.

3. Results and Discussion

3.1. Characterizations of Spherical HA Absorbent

Figure 1a,b shows the SEM images of the citric acid-assisted synthesized HA adsorbent. Different from the whisker-like HA reported in the literature, the product obtained with citric acid addition exhibited an interconnected porous microsphere structure [25]. This morphology is primarily attributed to the role of citric acid as a chelating agent, which can regulate the directional release of Ca^{2+} ions and induce the self-assembly of HA along the CO_2 bubble interface during the hydrothermal process [25]. These HA porous microspheres had a diameter ranging from approximately 1.9 μm to 5 μm, with a rough surface uniformly distributed with numerous pores. The chemical composition of the porous HA microspheres was determined by EDS, and the results are presented in Figure 1c. It can be seen that the sample was mainly composed of O, P, and Ca elements, along with a small amount of C element.

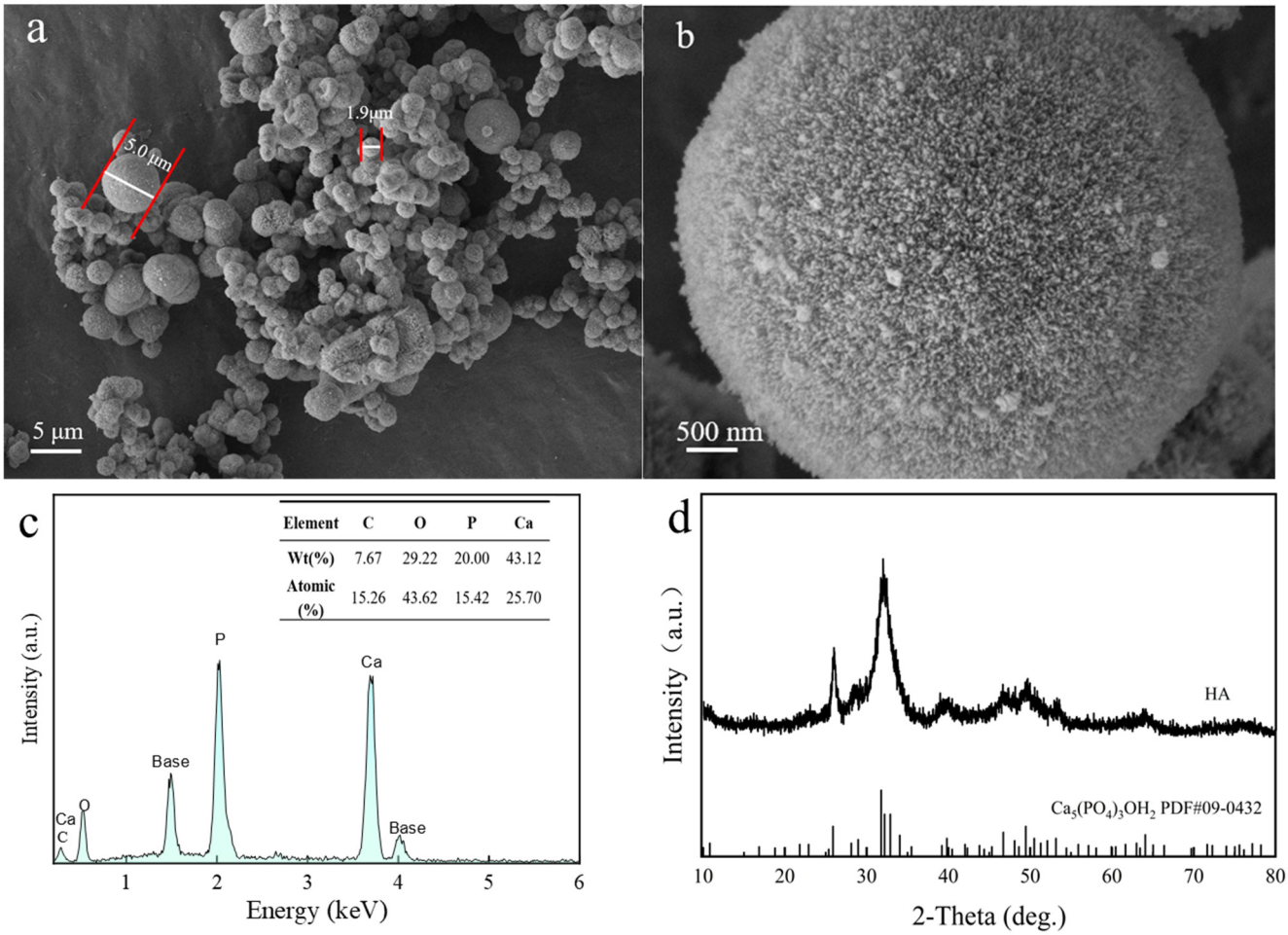

Figure 1. (**a**,**b**) SEM images, (**c**) EDS spectrum, and (**d**) XRD pattern of HA porous microspheres.

The crystalline phase of the sample was further examined using XRD. As shown in Figure 1d, the diffraction peaks of the HA porous microspheres at 21.93°, 26.03°, 31.95°, 32.27°, 33.09° and 49.62° can be assigned to the (200), (002), (211), (112), (300) and (213) planes of hexagonal HA (JCPDS 86-0740) [26]. In contrast to highly crystalline HA, the distinct diffraction peaks for the (211), (112), and (300) planes merged into a broad peak. The broadened diffraction peak indicates that the prepared HA porous microspheres exhibited low crystallinity. Previous studies have shown that low crystallinity can increase the specific surface area and active sites of HA, thereby significantly enhancing its adsorption capacity for heavy metal ions [27].

The functional groups on the HA porous microspheres were further characterized by FTIR. As exhibited in Figure 2, besides the band for incorporated water molecules (1601 cm^{-1}), the broad band at 3430 corresponds to the stretching vibration of –OH groups in HA. The peaks presenting at 1034, 961, 603, and 564 cm^{-1} are ascribed to the bending vibrations of O–P–O bonds. Notably, characteristic peaks of CO_3^{2-} vibration (at 1414 and 876 cm^{-1}) were detected in the synthesized HA porous microspheres, which is consistent with the EDS results. This indicates that CO_3^{2-} ions, produced from the decomposition of urea or citric acid under hydrothermal conditions, are incorporated into the HA lattice and partially replace phosphate ions [25,28].

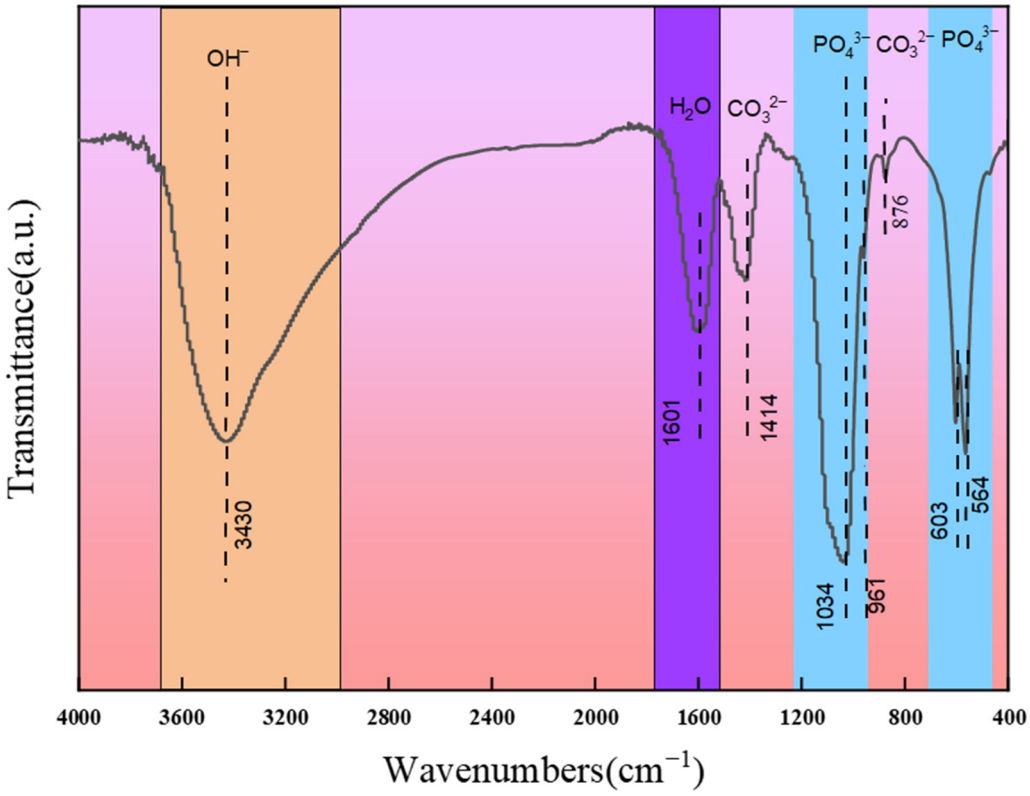

Figure 2. FTIR spectrum of the prepared HA porous microspheres.

Furthermore, the specific surface area of the prepared HA microspheres was investigated by nitrogen adsorption-desorption (Figure 3). The N_2 adsorption-desorption curve of the prepared HA exhibits a type-IV isotherm, which is characteristic of mesoporous materials. The pore size distribution was broad, ranging from 2 to 30 nm. The presence of larger pores could be due to the aggregation of HA microspheres, which creates additional free space and forms interparticle pores. The specific surface area of the HA microspheres was determined to be 207 m^2/g, which is considerably higher than that of other HA materials reported in the literature, such as 118 m^2/g and 30.8 m^2/g [29,30]. The combination of large pore volume and high specific surface area provides ample space for contact and reaction, which is conducive to enhancing the adsorption performance of HA porous microspheres toward Cu^{2+}.

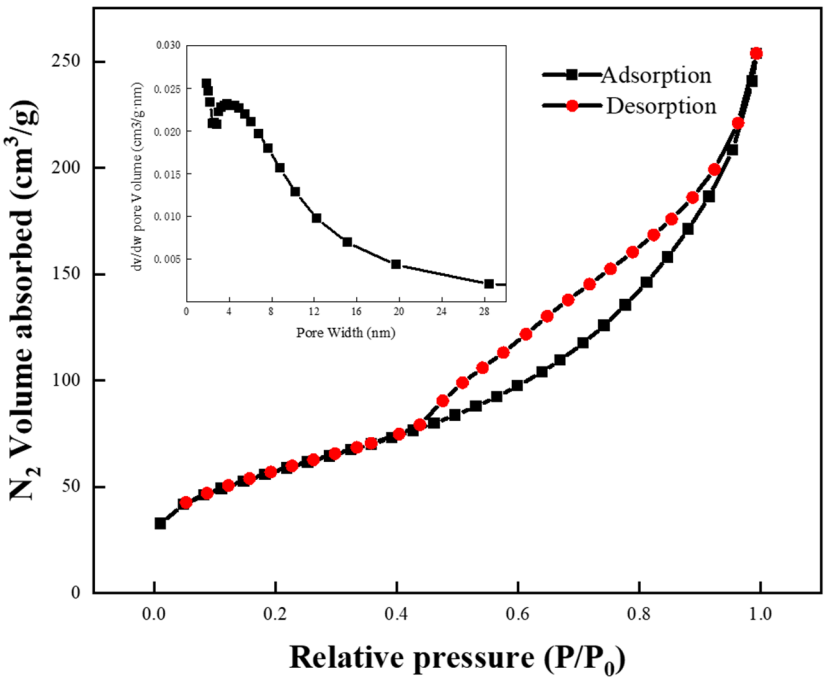

Figure 3. N_2 adsorption-desorption isotherm with pore size distribution of HA porous microspheres.

3.2. Adsorption Properties of HA Microsphere for Cu^{2+}

3.2.1. Effect of Dosage on Cu^{2+} Removal

The dosage of adsorbent is an important parameter that determines the solid-to-liquid ratio for efficient material utilization. The effect of dosage on the adsorption capacity of the HA porous microspheres was investigated, as shown in Figure 4. Clearly, as the HA porous microspheres dosage increased from 0.2 to 1.2 g/L, the adsorption capacity gradually decreased from 401 to 82 mg/g, while the corresponding removal efficiency increased from 80.20% to 97.88%. This is because increasing the adsorbent dosage results in Cu^{2+} ions being distributed across more porous microspheres, thereby reducing the adsorption capacity of the unit adsorbent [31]. However, increasing the dosage of HA porous microspheres provides more adsorption sites, thereby enabling more efficient adsorption of Cu^{2+} ions. Notably, the most significant improvement in adsorption efficiency occurred at a dosage of 0.8 g/L. Therefore, 0.8 g/L was selected as the optimal adsorbent dosage for the subsequent experiments.

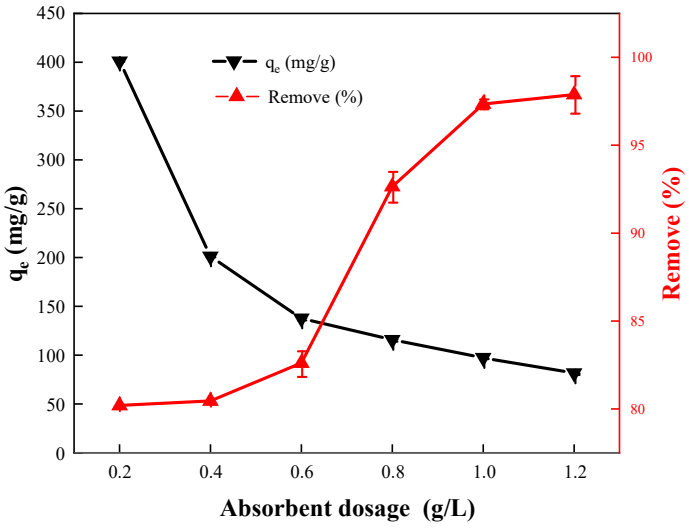

Figure 4. The effect of the dosage of the porous microspheres on the removal of Cu^{2+} ions ($[Cu^{2+}]_0$ = 100 mg/L, pH = 5.5, T = 298 K).

3.2.2. Effect of pH on Cu^{2+} Removal

Solution pH is considered to be a primary factor influencing the adsorption performance of the surface properties of the adsorbent [32]. The effect of initial pH (3–5) on Cu^{2+} removal was investigated, avoiding pH > 6 to prevent Cu^{2+} precipitation. The zeta potential of the HA porous microspheres was measured to be +3.48 (Figure 5a). As shown in Figure 5b, the adsorption capacity of the HA porous microspheres for Cu^{2+} increased from 91 mg/g to 115 mg/g as the pH rose from 3 to 5, with the corresponding removal efficiency increasing from 73% to 92%. The low adsorption capacity at pH 3 is primarily attributed to electrostatic repulsion between the Cu^{2+} cations and the positively charged adsorbent surface. The gradual enhancement of adsorption from pH 4.0 to 5.0 indicates that electrostatic attraction promotes the adsorption of Cu^{2+}. However, a considerable adsorption capacity of 91 mg/g was still observed even under unfavorable electrostatic repulsion at pH 3. This suggests that although electrostatic interactions exist, they are not the predominant mechanism, and their overall contribution to the overall adsorption process is limited.

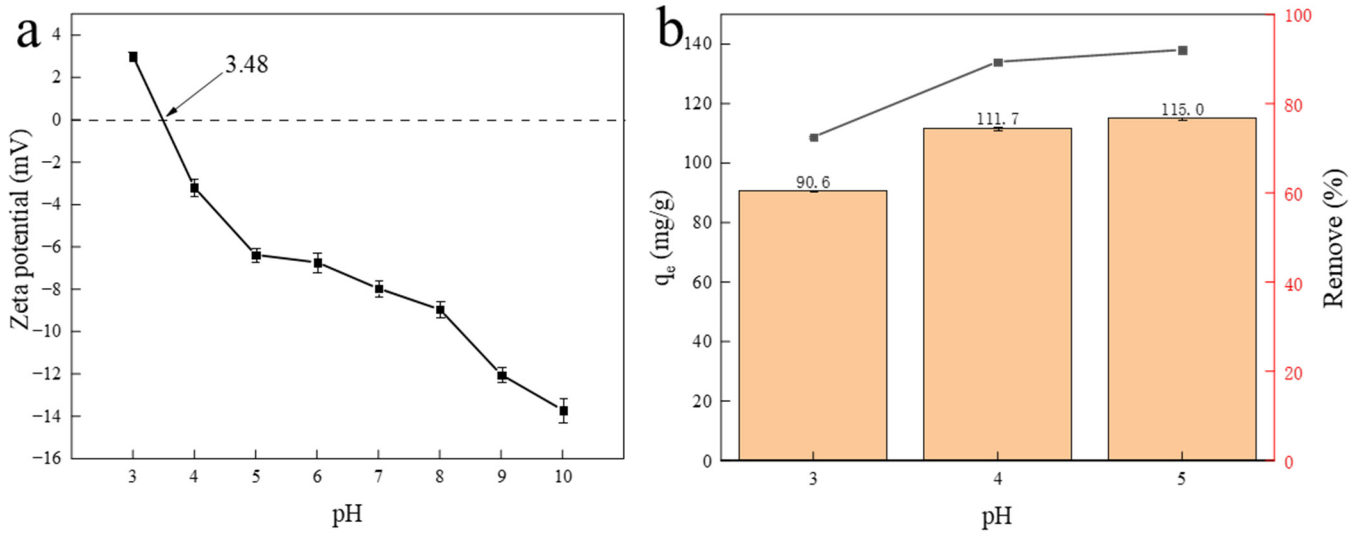

Figure 5. (**a**) The zeta potential curve of HA porous microspheres and (**b**) the effect of initial pH on the adsorption of Cu^{2+} adsorption by HA porous microspheres. ($[Cu^{2+}]_0$ = 100 mg/L, [HA dosage] = 0.8 g/L, T = 298 K).

3.2.3. Adsorption Isotherm

Adsorption isotherms describe the relationship between the adsorbate's adsorption capacity and its equilibrium concentration. The experimental data were fitted using the Langmuir, Freundlich, and Sips isotherm models. The Langmuir model describes monolayer adsorption onto a homogeneous surface, whereas the Freundlich model assumes multi-layer adsorption on heterogeneous surfaces [33,34]. The Sips isotherm model integrates the single-layer saturated adsorption concept of the Langmuir model with the heterogeneous description capability of the Freundlich model, making it suitable for describing single-layer adsorption behavior occurring on heterogeneous adsorbent surfaces [35]. The adsorption isotherm of Cu^{2+} on the HA porous microspheres is presented in Figure 6, and the corresponding calculated adsorption constants are listed in Table 1. As depicted in Figure 6a, the adsorption capacity exhibits a positive correlation with copper concentration before reaching equilibrium at C_0 = 300 mg/L (140.9 mg/g). This behavior confirms that the HA microspheres provide numerous surface adsorption sites, which eventually become saturated due to the finite availability of active sites [36,37]. As shown in Table 1, the Sips model exhibited the highest correlation coefficient (R^2 = 0.9957) among the three models. Furthermore, the *n* parameter of the Sips model was less than 1, revealing that the adsorption occurred on a heterogeneous surface with a broad distribution of adsorption site energies [38]. The maximum adsorption capacity

calculated from the Sips isotherm model was as high as 151.1 mg/g, which is attributed to the large pore volume and high specific surface area of the HA porous microspheres.

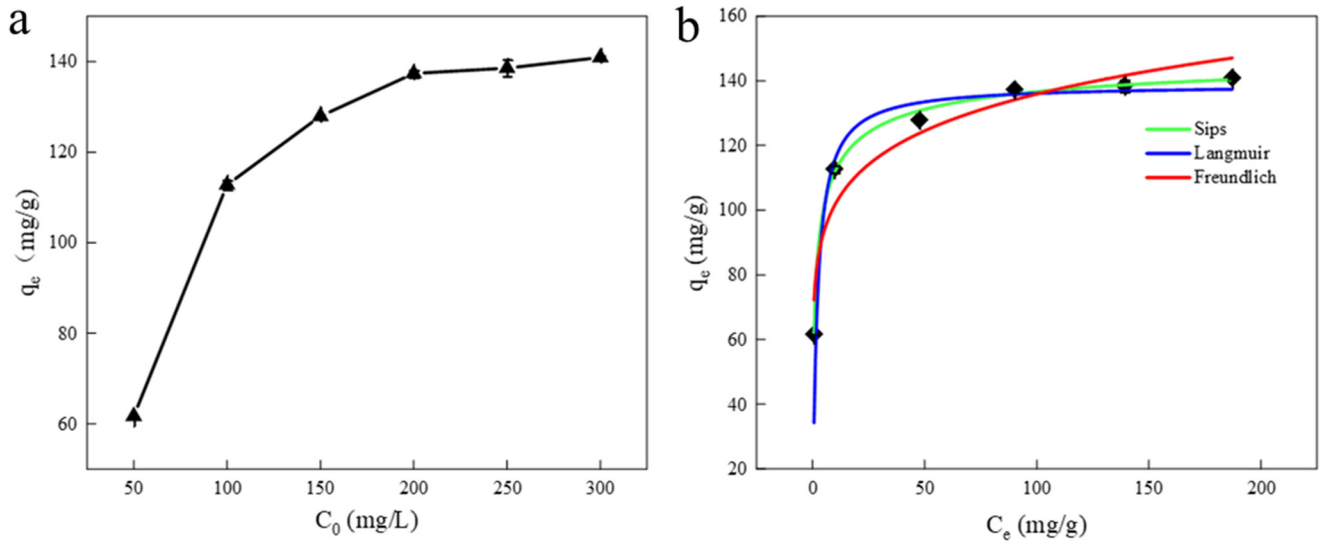

Figure 6. (**a**) Effect of initial concentration on adsorption capacity ([HA dosage] = 0.8 g/L, initial pH =5.5, T = 298 K), (**b**) isotherm curves for the adsorption of Cu^{2+} onto HA porous microspheres.

Table 1. Langmuir, Freundlich, and Sips isotherm parameters for the removal of Cu^{2+} removal by HA porous microspheres.

Isotherm	Parameters	Value
Langmuir	q_m (mg/g)	138.25
	K_L (L/mg)	1.15
	R^2	0.9043
Freundlich	K_F (mg/g(L/mg)$^{1/n}$)	65.80
	$1/n$	0.1525
	R^2	0.9145
Sips	K_S	0.7555
	q_m (mg/g)	151.13
	n	0.5189
	R^2	0.9957

3.2.4. Adsorption Kinetics

To understand the adsorption kinetics of Cu^{2+} on the HA porous microspheres, the effect of reaction time on the removal process was investigated. As shown in Figure 7a, the adsorption capacity for Cu^{2+} increased rapidly in the initial stage and then rose gradually until reaching equilibrium at approximately 300 min. The initial rapid removal is attributed to the abundant availability of the surface sites and pores on the HA microspheres. The subsequent gradual increase is attributed to progressive saturation of active sites and to potential pore blocking over time. The equilibrium adsorption capacity of the HA porous microspheres for Cu^{2+} was 116 mg/g, indicating that it is an effective adsorption material for Cu^{2+} removal. The kinetic data were fitted with pseudo-first-order and pseudo-second-order models to elucidate the adsorption mechanism. The kinetic model parameters and fitting curves are exhibited in Figure 7b,c. The results showed that the correlation coefficient (R^2) of the pseudo-second-order kinetic model was 0.9997, which was significantly higher than that of the pseudo-first-order kinetic model (R^2 = 0.9480). Furthermore, the calculated equilibrium adsorption capacity ($q_{e,cal}$, 117.37 mg/g) calculated by the pseudo-second-order model was in close agreement with the experimental value ($q_{e,exp}$, 116 mg/g). These findings indicate that the adsorption of Cu^{2+} onto the HA porous microspheres is predominantly governed by chemical adsorption [39].

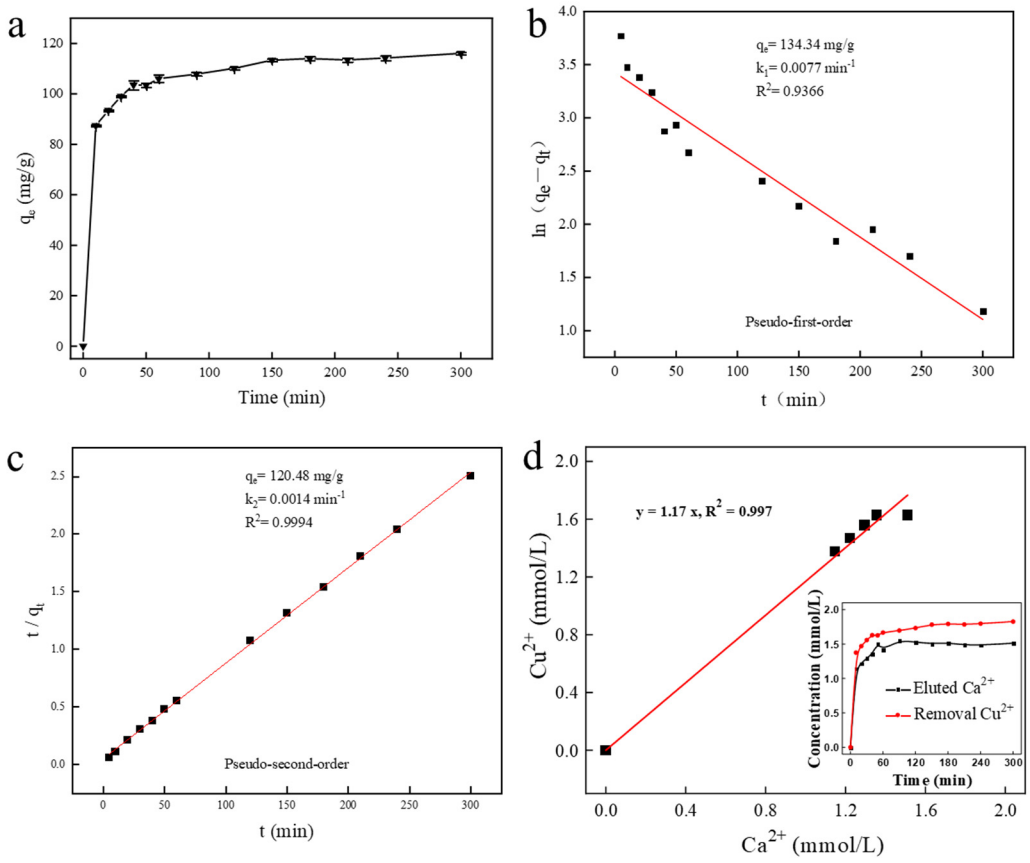

Figure 7. (**a**) Kinetic plot of Cu^{2+} removal by HA porous microspheres and the fitting curve based on (**b**) Pseudo-first order and (**c**) Pseudo-second-order models. ($[Cu^{2+}]_0$ = 100 mg/L, [HA dosage] = 0.8 g/L, pH = 5.5, T = 298 K). (**d**) Relationship between the removed Cu^{2+} and released Ca^{2+} concentration.

It has been reported that ion exchange is one of the primary mechanisms for the adsorption of heavy metals by HA [31]. To verify the role of ion exchange in the adsorption of Cu^{2+} by the prepared HA porous microspheres, the concentration of Ca^{2+} released into the solution was monitored during the adsorption process (inset of Figure 7d). Since the dissolution concentration of Ca^{2+} stabilized after 50 min, data from the first 50 min of the reaction were selected for detailed analysis. As shown in Figure 7d, the concentration of released Ca^{2+} was plotted against the amount of adsorbed Cu^{2+}, which yielded a linear correlation (R^2 = 0.997). This result confirms that ion exchange is a critical pathway governing the effective removal of Cu^{2+} by HA, which is also consistent with the kinetic fitting results [31]. Furthermore, to evaluate the adsorption performance of HA porous microspheres, their adsorption capacity was compared with that of recently reported HA-based adsorbents (Table 2). The equilibrium adsorption capacity of the HA porous microspheres for Cu^{2+} significantly exceeded the values reported in the literature (typically ranging from 25 to 99 mg/g), highlighting its exceptional Cu^{2+} adsorption performance and practical application potential.

Table 2. The comparison of Cu^{2+} adsorption between the prepared HA porous microspheres and the reported HA-based adsorbents.

Material	Adsorption Time	Adsorption Capacity (q_e, mg/g)	References
Hydroxyapatite/biochar nanocomposites	8 h	49.81	[31]
HA nanosheets	3 h	31.6	[22]
Pig-bone-based biochars	24 h	71.60	[40]
Hot ethanol treatment of HA	24 h	58.51	[41]
Biogenic hydroxyapatite	12 h	79.44	[42]
$CaCO_3$/chitin hydrogel	12 h	36.42	[43]
Magnetic composite microspheres	1.67 h	58.26	[44]

Cellulose microfibrils-grafted-hydroxyapatite	1 h	39.24	[45]
HA-coated calcite micro-particles	24 h	44.05	[46]
Biochar modified by hydroxyapatite	24 h	88.66	[47]
Zein (a kind of gliadin extracted)/PVA (polyvinyl alcohol)/HA	12 h	25.73	[48]
Spherical hydroxyapatite	5 h	116.07	This work

3.2.5. Adsorption Thermodynamics

The thermodynamic parameters for the adsorption of Cu^{2+} onto the HA porous microspheres are plotted in Figure 8 and summarized in Table 3. The positive value of ΔH^{o} indicates that the adsorption process was endothermic. The positive value of ΔS^{o} suggests an increase in randomness at the solid-solution interface, implying that the adsorption process is entropy-driven [49]. This entropy increase can be attributed to two primary factors: (i) the release of Ca^{2+} ions from the HA porous microspheres into the solution during ion exchange with Cu^{2+}, and (ii) the release of water molecules from the hydration shell of Cu^{2+} ions upon their fixation onto the solid surface [40]. Furthermore, the negative values of ΔG^{o} confirm that the adsorption of Cu^{2+} is spontaneous. The fact that ΔG^{o} became more negative with increasing temperature indicates that the spontaneity and extent of adsorption are enhanced at higher temperatures [50].

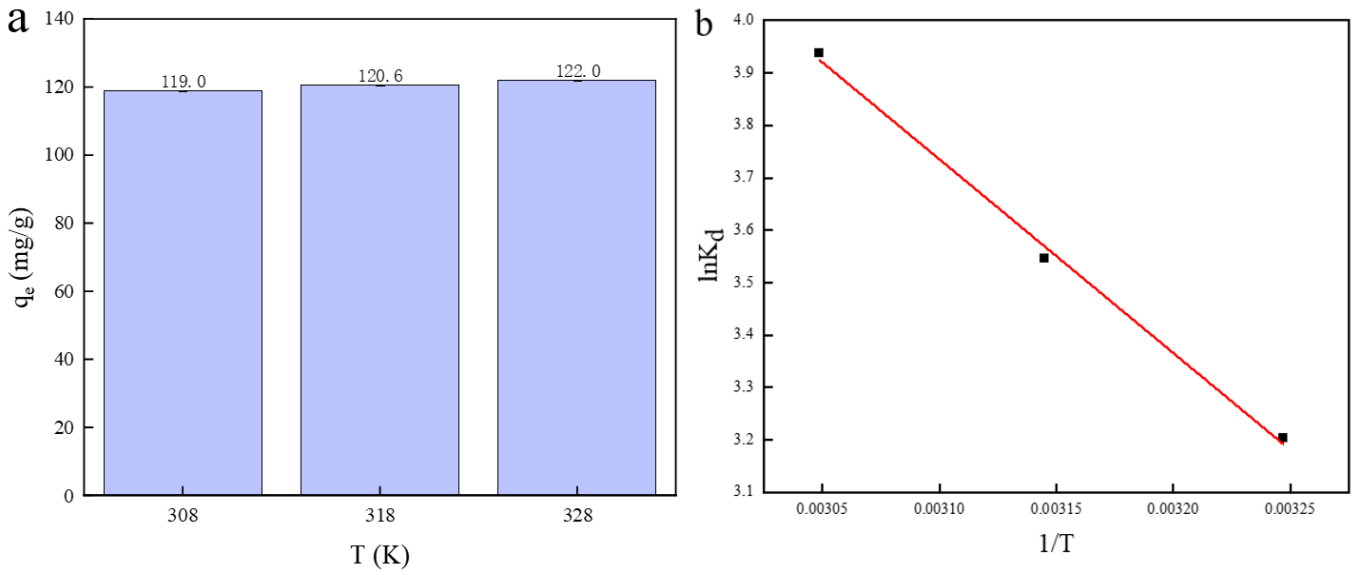

Figure 8. Effects of different temperatures on (**a**) the adsorption of Cu^{2+}; (**b**) Van't Hoff plot for the adsorption of Cu^{2+} on HA porous microspheres.

Table 3. Thermodynamic adsorption parameters for HA porous microspheres.

Temperature (K)	ΔH^{o} (kJ/mol)	ΔS^{o} (J/(mol·K))	ΔG^{o} (kJ/mol)
308	30.73	126.31	−8.21
318			−9.37
328			−10.74

3.2.6. Effect of Coexisting Cations

Wastewater often contains various cations that compete with copper ions for adsorption sites; therefore, it is crucial to investigate the influence of these cations on the adsorption selectivity of copper ions. By introducing 10 mg/L of anions into a pre-prepared Cu^{2+} solution, the effects of common aquatic cations—specifically K^{+}, Na^{+}, Mg^{2+}, and Ca^{2+}—on copper ion adsorption were examined. As illustrated in Figure 9, the presence of K^{+}, Na^{+}, Mg^{2+}, and Ca^{2+} did not significantly impact the adsorption of copper ions; this is

likely because copper exhibits a higher priority during the competitive adsorption process [45]. Consequently, it can be concluded that the synthesized HA demonstrates selectivity toward copper in water bodies and is capable of effectively remediating copper contamination in water.

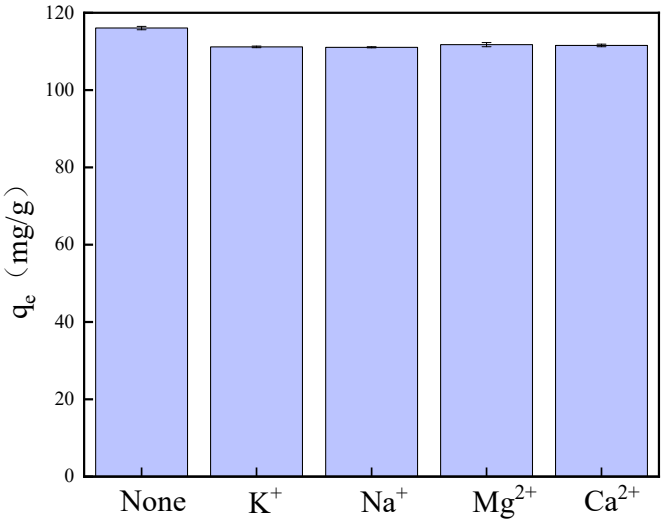

Figure 9. The Effect of Coexisting Cations on Cu^{2+} Adsorption.

3.3. Adsorption Mechanism

To elucidate the adsorption mechanism of Cu^{2+} on the HA porous microspheres, the adsorbent after Cu^{2+} adsorption (denoted as HA-Cu) was characterized by XRD, FTIR, and XPS. As shown in Figure 10a, no new diffraction peaks appeared in the XRD pattern of HA-Cu; however, the maximum diffraction peak shifted to a higher angle. This phenomenon is likely attributed to ion exchange, during which Cu^{2+} substitutes for Ca^{2+} in the HA crystal lattice. The smaller ionic radius of Cu^{2+} (~0.72 Å) compared to that of Ca^{2+} (~0.99 Å) induces a lattice contraction in the HA structure. The ion exchange reaction is represented by Equation (11). Furthermore, the significant amount of Ca^{2+} released into the solution observed during the kinetic studies provides experimental evidence for the ion exchange mechanism.

$$Ca_{10}(PO_4)_6(OH)_2 + xCu^{2+} \rightarrow Ca_{(10-x)}Cu_x(PO_4)_6(OH)_2 + xCa^{2+} \quad (11)$$

To further investigate the changes in surface functional groups, the FTIR spectrum of HA-Cu was analyzed, and the result is presented in Figure 10b. The intensity of the absorption peaks corresponding to the –OH groups at 3430 cm^{-1} and the PO_4^{3-} groups at 1034, 961, 603, and 564 cm^{-1} were slightly reduced after adsorption. The decrease in peak intensity suggests the occurrence of a surface complexation reaction between Cu^{2+} and the –OH/PO_4^{3-} groups on the HA microspheres [40,51], a mechanism that will be further discussed in the following section. Furthermore, the morphology and surface elemental distribution of the used adsorbent were examined by SEM and EDS mapping (Figure 10c–g). While no significant morphological change was observed, the presence of Cu element was detected on the surface, confirming the successful adsorption of Cu^{2+} onto the HA porous microspheres.

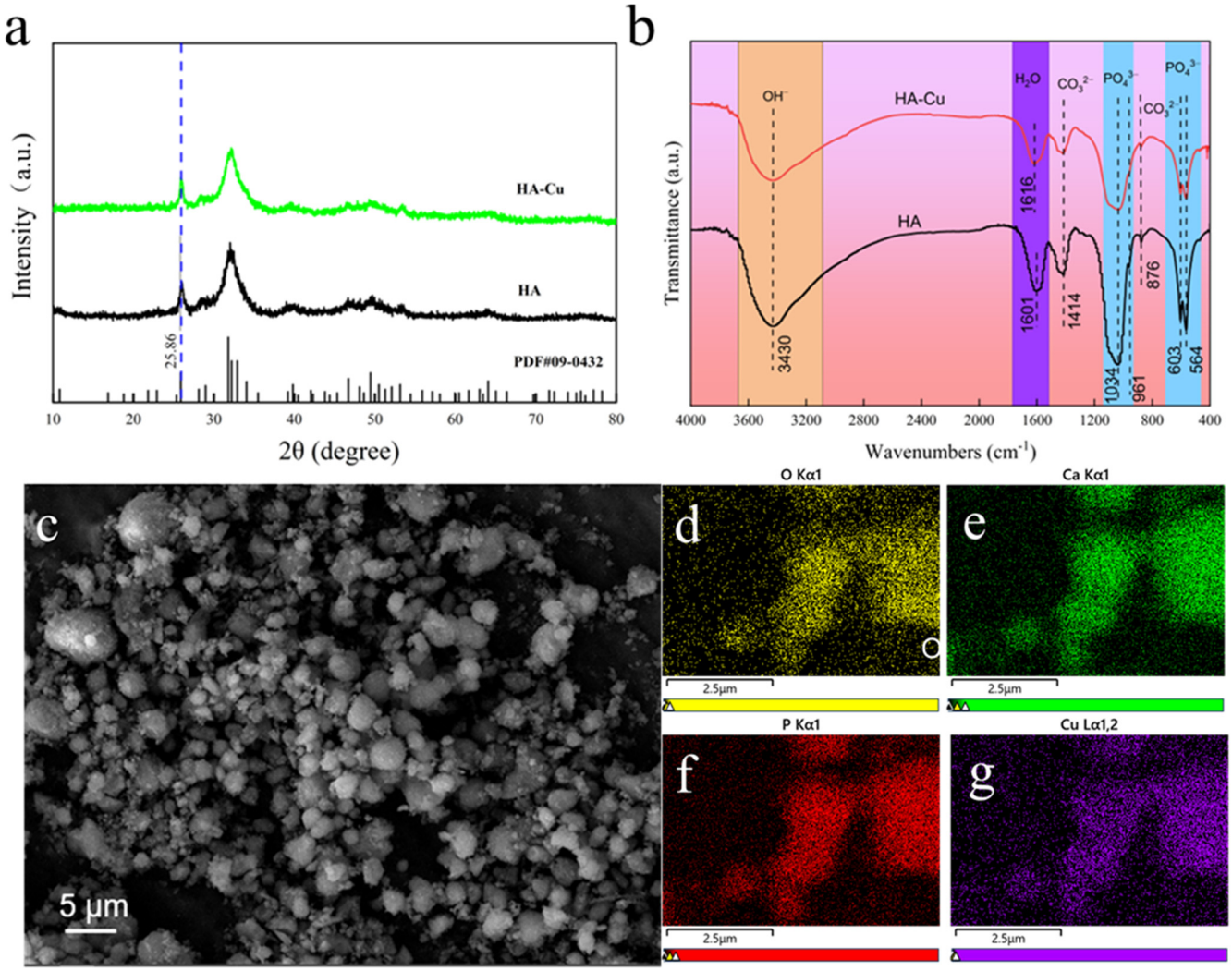

Figure 10. (**a**) XRD pattern, (**b**) FTIR spectra, (**c**) SEM images, and (**d**–**g**) corresponding element mapping images of HA porous microspheres after adsorption of Cu^{2+} ions.

XPS was employed to analyze the surface chemical composition of the HA porous microspheres before and after Cu^{2+} adsorption, and the results are presented in Figure 11. The survey spectrum (Figure 11a) revealed the appearance of new peaks corresponding to Cu, confirming the successful adsorption of Cu^{2+} onto the HA porous microspheres [52]. Concurrently, a significant decrease in the intensity of the Ca peaks was observed, indicating a reduction in surface Ca content. This observation is attributed to the ion exchange between Ca^{2+} in HA and Cu^{2+} in solution. The high-resolution O 1s spectrum (Figure 11b) was deconvoluted into three component peaks at binding energies of 530.86 eV, 532.45 eV, and 533.65 eV, which are assigned to M–OH (M = metal), C=O/P=O, and C–O/P–O bonds, respectively [28]. After Cu^{2+} adsorption, the M–OH peak shifted by 0.34 eV to a lower binding energy, and its relative peak area decreased from 86.54% to 84.68%. This consumption and shift of the M–OH peak may be attributed to the complexation between deprotonated hydroxyl groups and Cu^{2+} (Equations (12) and (13)) [40,53]. Furthermore, the peaks for C=O/P=O and C–O/P–O also shifted to lower binding energies (by 0.58 eV and 0.59 eV, respectively), while their relative peak areas increased from 10.73% to 11.79% and from 2.73% to 3.53%. These changes collectively indicate that oxygen-containing functional groups, including C=O/P=O, play a crucial role in the adsorption process.

$$\equiv Ca\text{-}OH_2^+ \leftrightarrow \equiv Ca\text{-}OH^0 + H^+ \quad (12)$$

$$\equiv P\text{-}O^{-} + H^{+} \leftrightarrow \equiv P\text{-}OH \quad (13)$$

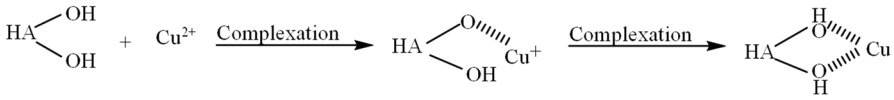

(14)

Figure 11c shows the P 2p spectra of the HA porous microspheres before and after Cu^{2+} adsorption. Similar to the O 1s spectrum, the P 2p spectrum of HA-Cu shifted to a lower binding energy. This change is not attributable to the formation of calcium phosphate precipitates, as XRD analysis revealed no formation of new phases, and the post-adsorption SEM images showed no significant changes in morphology; therefore, the adsorption process is not based on a dissolution-precipitation mechanism [54]. These observed shifts in both the O 1s and P 2p spectra can be attributed to a deprotonation process on the HA surface, as described by Equations (12) and (13) [55,56]. Specifically, the surface $\equiv Ca\text{-}OH_2^+$ and $\equiv P\text{-}OH$ groups undergo deprotonation at pH = 5.5. The resulting deprotonated groups then form complexes with Cu^{2+}, thereby enhancing the adsorption capacity of the HA microspheres [57]. Furthermore, the high-resolution Cu 2p spectrum was analyzed to confirm the chemical state of the adsorbed Cu (Figure 11d). The spectrum could be resolved into Cu $2p_{1/2}$ and Cu $2p_{3/2}$, confirming the successful adsorption of Cu^{2+} ions onto the HA surface [53]. Deconvolution of these peaks revealed the coexistence of both Cu^{2+} and Cu^{+} species. The presence of Cu^{2+} species is attributed to ion exchange with Ca^{2+}, while the Cu^{+} species arises from a surface complexation mechanism accompanied by electron transfer (Equation (14)) [58].

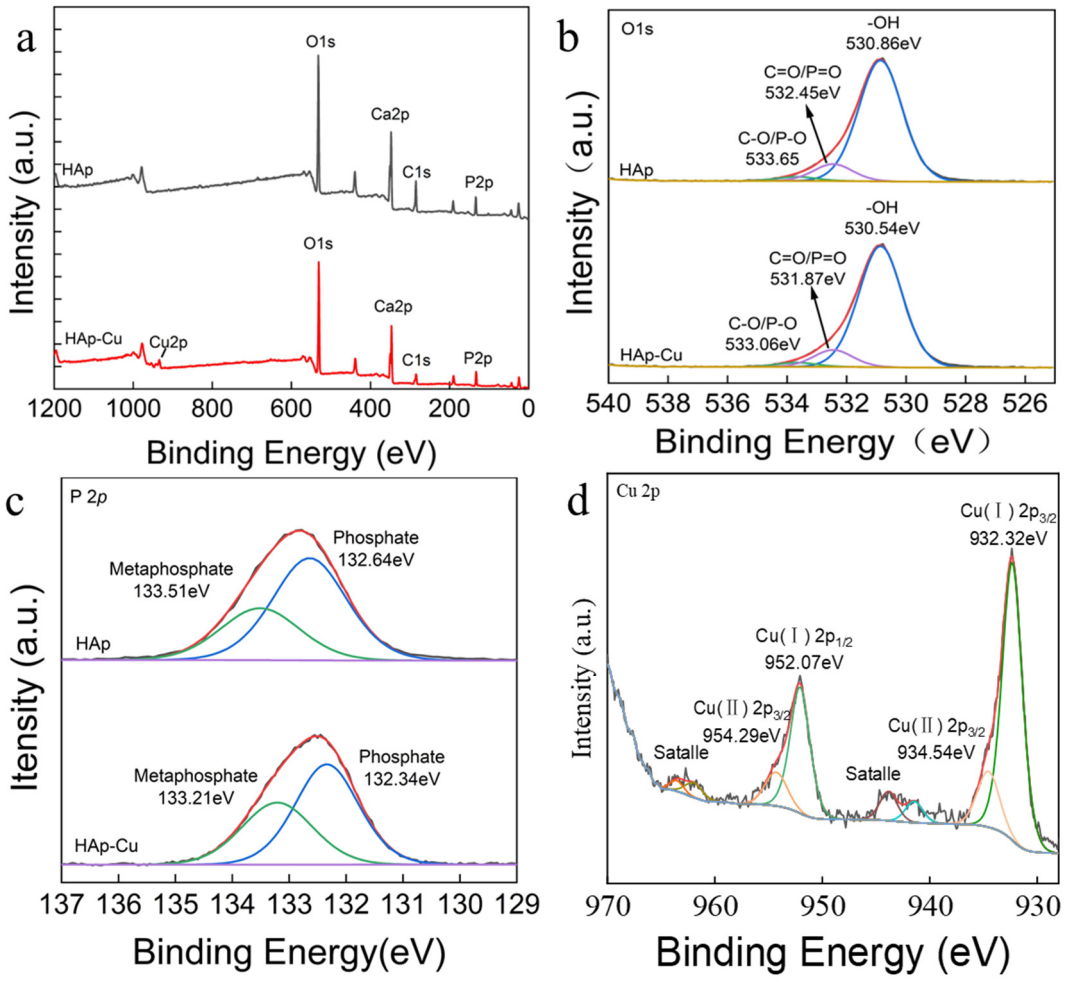

Figure 11. The XPS spectra of (**a**) survey scan, (**b**) O 1s, (**c**) P 2p, and (**d**) Cu 2p of HA porous microspheres before and after adsorption of Cu^{2+} ions.

In summary, the adsorption of Cu^{2+} ions by HA porous microspheres involves a complex process driven by multiple synergistic mechanisms (Figure 12). Specifically, ion exchange and surface complexation serve as the main pathways, while electrostatic interaction plays a minor role in the adsorption process. The high specific surface area and mesoporous structure of HA porous microspheres provide abundant active sites and promote efficient ion diffusion, significantly enhancing ion exchange and surface complexation. Consequently, these effects enhance the adsorption performance of HA porous microspheres for Cu^{2+} ions.

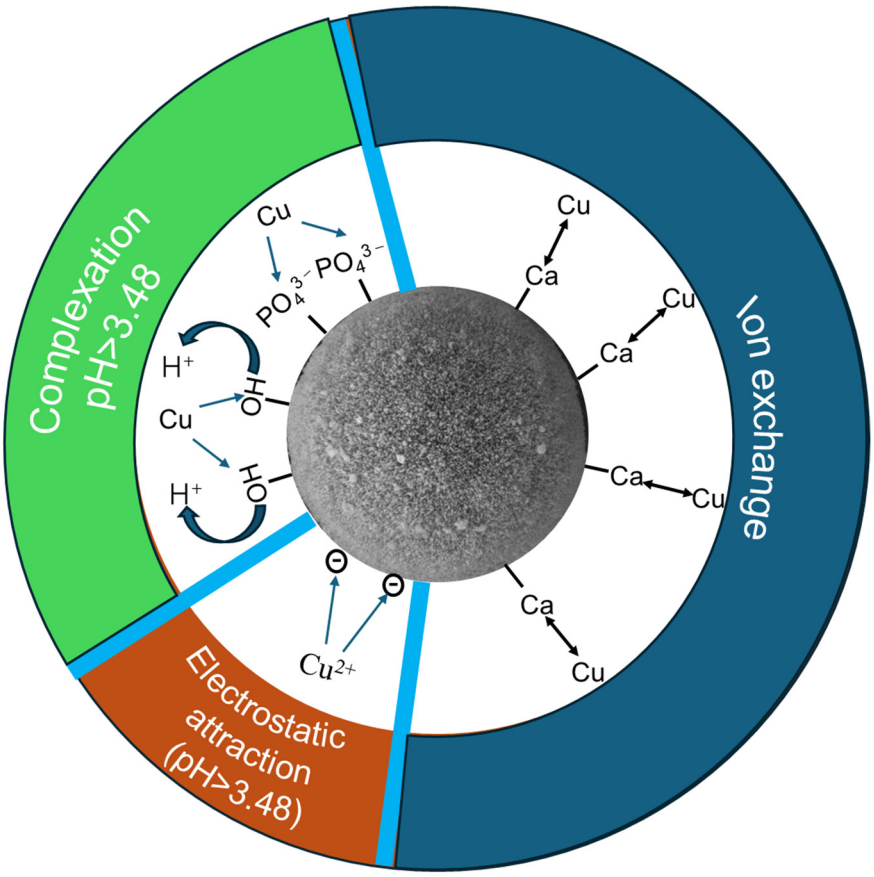

Figure 12. Schematic diagram illustrating the mechanism of Cu^{2+} adsorption by porous HA microspheres.

4. Conclusions

In conclusion, hydroxyapatite (HA) porous microspheres were successfully synthesized via a facile hydrothermal method. The prepared microspheres possessed a high specific surface area of 207 m^2/g and exhibited excellent adsorption performance for Cu^{2+}. The adsorption process followed the pseudo-second-order kinetic model and the Sips isotherm model. The fitting results indicated that the adsorption of Cu^{2+} was primarily a chemical adsorption process, with a maximum adsorption capacity of 116 mg/g. Combined experimental and characterization analyses revealed that ion exchange and surface complexation are the main mechanisms, while electrostatic interaction plays a minor role. The high specific surface area of the HA porous microspheres significantly increased the contact area with Cu^{2+}, thereby promoting ion exchange and surface complexation and leading to the enhanced adsorption capacity. This work provides a novel and efficient strategy for removing Cu^{2+} ions from wastewater using eco-friendly HA porous microspheres. Nevertheless, the susceptibility of this hydroxyapatite to dissolution in acidic environments limits its reusability. To better address the demands of actual wastewater treatment, future work will build upon this synthesis method by incorporating other materials to form composites with improved acid resistance.

Statement of the Use of Generative AI and AI-Assisted Technologies in the Writing Process

During the preparation of this manuscript, the authors used DeepSeek in order to improve the readability and language quality of the manuscript. After using this tool, the authors reviewed and edited the content as needed and take full responsibility for the content of the published article.

Author Contributions

Conceptualization, Q.Z.; Methodology, T.D.; Software, T.D.; Validation, R.C., J.Y. and W.Y.; Formal Analysis, T.D.; Investigation, T.D.; Resources, Q.Z.; Data Curation, T.D.; Writing—Original Draft Preparation, T.D.; Writing—Review & Editing, Z.H.; Visualization, J.Y.; Supervision, Q.Z.; Project Administration, R.C.; Funding Acquisition, Q.Z.

Ethics Statement

Not applicable.

Informed Consent Statement

Not applicable.

Data Availability Statement

The data presented in this study are available on request from the corresponding author.

Funding

The financial support from Natural Science Foundation of Hubei Province (No. 2024AFD141 and 2024AFD146) is acknowledged. The financial support from National Natural Science Foundation of China through grant No. 52372120 is acknowledged. This work was supported by the Wuhan Institute of Technology startup funding (No. 23QD40). This work was financially supported by the research funds of Key Laboratory of Textile Fiber and Products (Ministry of Education) through grant No. Fzxw2024009. This work was supported by Ministry of Education's Industry-University-Research Collaborative Education Program (No. 2408074419).

Declaration of Competing Interest

The authors declare that they have no known competing financial interests or personal relationships that could have appeared to influence the work reported in this paper.

References

1. Ma WC, Han R, Zhang W, Zhang H, Chen L, Zhu L. Magnetic biochar enhanced copper immobilization in agricultural lands: Insights from adsorption precipitation and redox. *J. Environ. Manage.* **2024**, *352*, 120058. DOI:10.1016/j.jenvman.2024.120058
2. Ozdemir S, Turkan Z, Kilinc E, Bayat R, Soylak M, Sen F. Preconcentrations of Cu (II) and Mn (II) by magnetic solid-phase extraction on Bacillus cereus loaded γ-Fe_2O_3 nanomaterials. *Environ. Res.* **2022**, *209*, 112766. DOI:10.1016/j.envres.2022.112766
3. Hopkins DT, MacQuarrie S, Hawboldt KA. Removal of copper from sulfate solutions using biochar derived from crab processing by-product. *J. Environ. Manage.* **2022**, *303*, 114270. DOI:10.1016/j.jenvman.2021.114270
4. Wei YF, Chen T, Qiu ZY, Liu H, Xia Y, Wang Z, et al. Enhanced lead and copper removal in wastewater by adsorption onto magnesium oxide homogeneously embedded hierarchical porous biochar. *Bioresour. Technol.* **2022**, *365*, 128146. DOI:10.1016/j.biortech.2022.128146
5. Shrestha R, Ban S, Devkota S, Sharma S, Joshi R, Tiwari AP, et al. Technological trends in heavy metals removal from industrial wastewater: A review. *J. Environ. Chem. Eng.* **2021**, *9*, 105688. DOI:10.1016/j.jece.2021.105688

6. Babeker TMA, Lv S, Khalil MN, Hao Z, Chen Q. Biochar modified by ammonium pyrrolidine dithiocarbamate for high selective adsorption of copper in wastewater. *Sep. Purif. Technol.* **2025**, *354*, 129436. DOI:10.1016/j.seppur.2024.129436
7. Lin SY, Liu XY, Ma HQ, Liu YZ, Wang Y, Liu H, et al. Fe/Mn/Zr ternary electrode facilitates ultra-low-resistance electrocatalysis for closed-loop electrochemical removal of heavy metals from industrial wastewater. *Chem. Eng. J.* **2025**, *525*, 170397. DOI:10.1016/j.cej.2025.170397
8. Cao QQ, Huang ZH, Liu SG, Wu YP. Potential of Punica granatum biochar to adsorb Cu (II) in soil. *Sci. Rep.* **2019**, *9*, 11116. DOI:10.1038/s41598-019-46983-2
9. Shen XY, Chi YK, Xiong KN. The effect of heavy metal contamination on humans and animals in the vicinity of a zinc smelting facility. *PLoS ONE* **2019**, *14*, e0207423. DOI:10.1371/journal.pone.0207423
10. Pu XQ, Yao L, Yang L, Jiang WJ, Jiang X. Utilization of industrial waste lithium-silicon-powder for the fabrication of novel nap zeolite for aqueous Cu (II) removal. *J. Clean. Prod.* **2020**, *265*, 121822. DOI:10.1016/j.jclepro.2020.121822
11. Guemiza K, Coudert L, Metahni S, Mercier G, Besner S, Blais J-F. Treatment technologies used for the removal of As, Cr, Cu, PCP and/or PCDD/F from contaminated soil: A review. *J. Hazard. Mater.* **2017**, *333*, 194–214. DOI:10.1016/j.jhazmat.2017.03.021
12. Wang C, Xiong C, He YL, Yang C, Li X, Zheng J, et al. Facile preparation of magnetic Zr-MOF for adsorption of Pb (II) and Cr (VI) from water: Adsorption characteristics and mechanisms. *Chem. Eng. J.* **2021**, *415*, 128923. DOI:10.1016/j.cej.2021.128923
13. Zhang Z, Wang T, Zhang HX, Liu Y, Xing B. Adsorption of Pb (II) and Cd (II) by magnetic activated carbon and its mechanism. *Sci. Total Environ.* **2021**, *757*, 143910. DOI:10.1016/j.scitotenv.2020.143910
14. White RL, White CM, Turgut H, Massoud A, Tian ZR. Comparative studies on copper adsorption by graphene oxide and functionalized graphene oxide nanoparticles. *J. Taiwan Inst. Chem. Eng.* **2018**, *85*, 18–28. DOI:10.1016/j.jtice.2018.01.036
15. Rodríguez RP, Alfonso Herrera LÁ, Cervantes JM, Tapia AM, Chiñas Rojas LE, Rivera Villanueva JM. Highly efficient adsorption of aqueous heavy metals by Co-derived metal-organic framework. Synergistic mechanism for enhanced water purification. *J. Solid State Chem.* **2024**, *338*, 124833. DOI:10.1016/j.jssc.2024.124833
16. Nasir A, Inaam-ul-Hassan M, Raza A, Tahir M, Yasin T. Removal of copper using chitosan beads embedded with amidoxime grafted graphene oxide nanohybids. *Int. J. Biol. Macromol.* **2022**, *222*, 750–758. DOI:10.1016/j.ijbiomac.2022.09.188
17. Li ZL, Qiu Y, Zhao DY, Li J, Li G, Jia H, et al. Application of apatite particles for remediation of contaminated soil and groundwater: A review and perspectives. *Sci. Total Environ.* **2023**, *904*, 166918. DOI:10.1016/j.scitotenv.2023.166918
18. Zhou CL, Zhou QQ, Yu Y, Ge SF. Spongy magnetic hydroxyapatite for the enhanced Pb^{2+} removal and its dynamic sorption mechanism. *J. Environ. Chem. Eng.* **2023**, *11*, 110213. DOI:10.1016/j.jece.2023.110213
19. Ibrahim M, Labaki M, Giraudon J-M, Lamonier J-F. Hydroxyapatite, a multifunctional material for air, water and soil pollution control: A review. *J. Hazard. Mater.* **2020**, *383*, 121139. DOI:10.1016/j.jhazmat.2019.121139
20. Wang T, Cao WY, Dong K, Li H, Wang D, Xu Y. Hydroxyapatite and its composite in heavy metal decontamination: Adsorption mechanisms, challenges, and future perspective. *Chemosphere* **2024**, *352*, 141367. DOI:10.1016/j.chemosphere.2024.141367
21. Wu HY, Ling LB, Wang T, Dong K, Xu Y, Yu G, et al. Temperature-Directed Morphological Tuning of Hydroxyapatite Nanowires and Dual-Stage Mechanism for Pb (II) Adsorption. *Environ. Res.* **2025**, *287*, 123145. DOI:10.1016/j.envres.2025.123145
22. Su YP, Wang J, Li S, Zhu JH, Liu WS, Zhang ZT. Self-templated microwave-assisted hydrothermal synthesis of two-dimensional holey hydroxyapatite nanosheets for efficient heavy metal removal. *Environ. Sci. Pollut. Res.* **2019**, *26*, 30076–30086. DOI:10.1007/s11356-019-06160-4
23. Lebre F, Sridharan R, Sawkins MJ, Kelly DJ, O'Brien FJ, Lavelle EC. The shape and size of hydroxyapatite particles dictate inflammatory responses following implantation. *Sci. Rep.* **2017**, *7*, 2922. DOI:10.1038/s41598-017-03086-0
24. Chen BY, Li CX, Song JQ, Dai XZ, Lu ZQ, Zhou ZH, et al. Removal of Cl-from contaminated acid by resin adsorption: Kinetics, isothermal model, approximate site energy distribution and adsorption mechanism. *J. Environ. Chem. Eng.* **2025**, *13*, 116656. DOI:10.1016/j.jece.2025.116656
25. Cheng XK, Huang ZL, Li JQ, Liu Y, Chen C, Chi R-A, et al. Self-assembled growth and pore size control of the bubble-template porous carbonated hydroxyapatite microsphere. *Cryst. Growth Des.* **2010**, *10*, 1180–1188. DOI:10.1021/cg901088c
26. Wang YC, Dai HL, Li ZH, Meng Z-Y, Xiao Y, Zhao Z. Mesoporous polydopamine-coated hydroxyapatite nano-composites for ROS-triggered nitric oxide-enhanced photothermal therapy of osteosarcoma. *J. Mater. Chem. B* **2021**, *9*, 7401–7408. DOI:10.1039/D1TB01084K

27. Stötzel C, Müller F, Reinert F, Niederdraenk F, Barralet J, Gbureck U. Ion adsorption behaviour of hydroxyapatite with different crystallinities. *Colloids Surf. B* **2009**, *74*, 91–95. DOI:10.1016/j.colsurfb.2009.06.031
28. Irawan V, Akaike K, Mizuno HL, Anraku Y, Sotome S, Okawa A, et al. Comparative study on the sintered porous A-type carbonate apatite, B-type carbonate apatite, and hydroxyapatite. *J. Am. Ceram. Soc.* **2025**, *108*, e20389. DOI:10.1111/jace.20389
29. Zhang JY, Xia X, Zeng LR, Zeng SY, Li KQ, Fang ZK, et al. New insights into the co-pyrolysis synergistic effect of pig bone-derived natural hydroxyapatite and sodium-rich Spartina alterniflora on forming highly active heterostructure sites for enhanced Cu^{2+} removal. *Sep. Purif. Technol.* **2025**, *364*, 132512. DOI:10.1016/j.seppur.2025.132512
30. Valenzuela EI, Sánchez-Urzúa JM, Mendoza PGY, Navarro-Márquez M, Zayas-Olivares A, Gutiérrez-Uribe JA, et al. Recovery of calcium from maize Lime-Cooking wastewater as hydroxyapatite for biomedical applications. *Sep. Purif. Technol.* **2025**, *365*, 132777. DOI:10.1016/j.seppur.2025.132777
31. Jung K-W, Lee SY, Choi J-W, Lee YJ. A facile one-pot hydrothermal synthesis of hydroxyapatite/biochar nanocomposites: Adsorption behavior and mechanisms for the removal of copper (II) from aqueous media. *Chem. Eng. J.* **2019**, *369*, 529–541. DOI:10.1016/j.cej.2019.03.102
32. Yang X, Zhang XL, Wang ZW, Li S, Zhao J, Liang G, et al. Mechanistic insights into removal of norfloxacin from water using different natural iron ore–biochar composites: more rich free radicals derived from natural pyrite-biochar composites than hematite-biochar composites. *Appl. Catal. B Environ.* **2019**, *255*, 117752. DOI:10.1016/j.apcatb.2019.117752
33. Allen SJ, Mckay G, Porter JF. Adsorption isotherm models for basic dye adsorption by peat in single and binary component systems. *J. Colloid Interface Sci.* **2004**, *280*, 322–333. DOI:10.1016/j.jcis.2004.08.078
34. Syafiuddin A, Salmiati S, Jonbi J, Fulazzaky MA. Application of the kinetic and isotherm models for better understanding of the behaviors of silver nanoparticles adsorption onto different adsorbents. *J. Environ. Manage.* **2018**, *218*, 59–70. DOI:10.1016/j.jenvman.2018.03.066
35. Dwivedi AD, Dubey SP, Gopal K, Sillanpää M. Strengthening adsorptive amelioration: Isotherm modeling in liquid phase surface complexation of Pb (II) and Cd (II) ions. *Desalination* **2011**, *267*, 25–33. DOI:10.1016/j.desal.2010.09.002
36. Du BY, Chai LF, Li W, Wang X, Chen XH, Zhou JH, et al. Preparation of functionalized magnetic graphene oxide/lignin composite nanoparticles for adsorption of heavy metal ions and reuse as electromagnetic wave absorbers. *Sep. Purif. Technol.* **2022**, *297*, 121509. DOI:10.1016/j.seppur.2022.121509
37. Lü LL, Jiang XJ, Jia L, Ai T, Wu H. Kinetic and thermodynamic studies on adsorption of Cu^{2+}, Pb^{2+}, methylene blue and malachite green from aqueous solution using AMPS-modified hazelnut shell powder. *Chem. Res. Chin. Univ.* **2017**, *33*, 112–118. DOI:10.1007/s40242-017-6243-6
38. Günay A, Arslankaya E, Tosun I. Lead removal from aqueous solution by natural and pretreated clinoptilolite: Adsorption equilibrium and kinetics. *J. Hazard. Mater.* **2007**, *146*, 362–371. DOI:10.1016/j.jhazmat.2006.12.034
39. Shi TZ, Xie ZF, Zhu Z, Shi W, Liu Y, Liu M. Highly efficient and selective adsorption of heavy metal ions by hydrazide-modified sodium alginate. *Carbohydr. Polym.* **2022**, *276*, 118797. DOI:10.1016/j.carbpol.2021.118797
40. Zhang JY, Xia X, Li KQ, Shen YF, Xue Y. New insights into temperature-induced mechanisms of copper adsorption enhancement on hydroxyapatite-in situ self-doped fluffy bread-like biochar. *Chem. Eng. J.* **2024**, *479*, 147657. DOI:10.1016/j.cej.2023.147657
41. Bazargan-Lari R, Zafarani HR, Bahrololoom ME, Nemati A. Removal of Cu (II) ions from aqueous solutions by low-cost natural hydroxyapatite/chitosan composite: Equilibrium, kinetic and thermodynamic studies. *J. Taiwan Inst. Chem. Eng.* **2014**, *45*, 1642–1648. DOI:10.1016/j.jtice.2013.11.009
42. Liu XF, Yin H, Liu H, Cai YH, Qi X, Dang Z. Multicomponent adsorption of heavy metals onto biogenic hydroxyapatite: Surface functional groups and inorganic mineral facilitating stable adsorption of Pb (II). *J. Hazard. Mater.* **2023**, *443*, 130167. DOI:10.1016/j.jhazmat.2022.130167
43. Dou DT, Wei DL, Guan X, Liang ZJ, Lan LH, Lan XD, et al. Adsorption of copper (II) and cadmium (II) ions by *in situ* doped nano-calcium carbonate high-intensity chitin hydrogels. *J. Hazard. Mater.* **2022**, *423*, 127137. DOI:10.1016/j.jhazmat.2021.127137
44. Yin H, Xiong QQ, Zhang M, Wang BW, Zhang FG. Multi-principles analysis of Cu (II) adsorption in water on magnetic microspheres and modified Chitosan. *J. Environ. Chem. Eng.* **2023**, *11*, 111285. DOI:10.1016/j.jece.2023.111285
45. Marrane SE, Danoun K, Allouss D, Sair S, Channab B-E, Rhihil A, et al. A novel approach to prepare cellulose-*g*-hydroxyapatite originated from natural sources as an efficient adsorbent for heavy metals: Batch adsorption optimization via response surface methodology. *ACS Omega* **2022**, *7*, 28076–28092. DOI:10.1021/acsomega.2c02108
46. Gibert O, Valderrama C, Martínez MM, Darbra RM, Moncunill JO, Martí V. Hydroxyapatite coatings on calcite powder for the removal of heavy metals from contaminated water. *Water* **2021**, *13*, 1493. DOI:10.3390/w13111493

47. Chen YN, Li ML, Li YP, Liu YH, Chen YR, Li H, et al. Hydroxyapatite modified sludge-based biochar for the adsorption of Cu^{2+} and Cd^{2+}: Adsorption behavior and mechanisms. *Bioresour. Technol.* **2021**, *321*, 124413. DOI:10.1016/j.biortech.2020.124413
48. Ma N, Li K, Xu B, Tian HF, Ma SB, Li JL, et al. Zein/polyvinyl alcohol-based electrospun nanofibrous films reinforced with nano-hydroxyapatite for efficient Cu (II) adsorption. *J. Appl. Polym. Sci.* **2024**, *141*, e55086. DOI:10.1002/app.55086
49. Yamsomphong K, Xu H, Yang P, Setyawan MIB, Yotpanya N, Yokoi T, et al. Excellent but strange adsorption performance of shrimp shell-derived adsorbent for anionic pollutant removal. *Chem. Eng. J.* **2025**, *515*, 163683. DOI:10.1016/j.cej.2025.163683
50. Kayalvizhi K, Alhaji N, Saravanakkumar D, Mohamed SB, Kaviyarasu K, Ayeshamariam A, et al. Adsorption of copper and nickel by using sawdust chitosan nanocomposite beads–A kinetic and thermodynamic study. *Environ. Res.* **2022**, *203*, 111814. DOI:10.1016/j.envres.2021.111814
51. Liao J, Xiong T, Ding L, Xie Y, Zhang Y, Zhu W. Design of a renewable hydroxyapatite-biocarbon composite for the removal of uranium (VI) with high-efficiency adsorption performance. *Biochar* **2022**, *4*, 29. DOI:10.1007/s42773-022-00154-1
52. Pavithra S, Thandapani G, Alkhamis HH, Alrefaei AF, Almutairi MH. Batch adsorption studies on surface tailored chitosan/orange peel hydrogel composite for the removal of Cr (VI) and Cu (II) ions from synthetic wastewater. *Chemosphere* **2021**, *271*, 129415. DOI:10.1016/j.chemosphere.2020.129415
53. Xu CQ, Liu Q, Han YW, Hu S, Xu S. Efficient adsorption of Cu^{2+} using ZnCo bimetallic organic frameworks loaded cellulose-based modified aerogel: Adsorption behavior and mechanism. *Environ. Res.* **2025**, *269*, 120877. DOI:10.1016/j.envres.2025.120877
54. Xiao X, Yang L, Zhou DL, Zhou JB, Tian YP, Song CS, et al. Magnetic γ-Fe_2O_3/Fe-doped hydroxyapatite nanostructures as high-efficiency cadmium adsorbents. *Colloid Surf. Physicochem. Eng. Asp.* **2018**, *555*, 548–557. DOI:10.1016/j.colsurfa.2018.07.036
55. Zhan YH, Lin JW, Li J. Preparation and characterization of surfactant-modified hydroxyapatite/zeolite composite and its adsorption behavior toward humic acid and copper (II). *Environ. Sci. Pollut. Res.* **2013**, *20*, 2512–2526. DOI:10.1007/s11356-012-1136-1
56. Yang L, Wei ZG, Zhong WH, Cui J, Wei W. Modifying hydroxyapatite nanoparticles with humic acid for highly efficient removal of Cu (II) from aqueous solution. *Colloid Surf. Physicochem. Eng. Asp.* **2016**, *490*, 9–21. DOI:10.1016/j.colsurfa.2015.11.039
57. Liao J, Ding L, Zhang Y, Zhu W. Efficient removal of uranium from wastewater using pig manure biochar: Understanding adsorption and binding mechanisms. *J. Hazard. Mater.* **2022**, *423*, 127190. DOI:10.1016/j.jhazmat.2021.127190
58. Zheng T, Wang T, Ma RQ, Liu W, Cui F, Sun W. Influences of isolated fractions of natural organic matter on adsorption of Cu (II) by titanate nanotubes. *Sci. Total Environ.* **2019**, *650*, 1412–1418. DOI:10.1016/j.scitotenv.2018.09.152